

Stratospheric balloon observations of comets C/2013 A1 (Siding Spring), C/2014 E2 (Jacques), and Ceres



Andrew F. Cheng^{a,*}, C.A. Hibbitts^a, R. Espiritu^a, R. McMichael^a, Z. Fletcher^a, P. Bernasconi^a, J.D. Adams^a, C.M. Lisse^a, M.L. Sitko^b, R. Fernandes^b, E.F. Young^c, T. Kremic^d

^aAPL, Laurel, Space 11100 Johns Hopkins Rd, MD 20723 United States

^bUniv. Cincinnati, OH, United States

^cSwRI, Boulder, CO, United States

^dNASA/GRC, United States

ARTICLE INFO

Article history:

Received 3 February 2016

Revised 27 July 2016

Accepted 4 August 2016

Available online 6 August 2016

Keywords:

Comets

Coma

Comets

Dust

Asteroid Ceres

Experimental techniques

ABSTRACT

The Balloon Observation Platform for Planetary Science (BOPPS) was launched from Fort Sumner, New Mexico on September 26, 2014 and observed Oort Cloud comets from a stratospheric balloon observatory, using a 0.8 meter aperture telescope, a pointing system that achieved < 1 arc second pointing stability, and an imaging instrument suite covering the near-ultraviolet to mid-infrared. BOPPS observed two Oort Cloud comets, C/2013 A1 (Siding Spring) and C/2014 E2 (Jacques), at the $2.7 \mu\text{m}$ wavelength of water emission. BOPPS also observed Ceres at $2.7 \mu\text{m}$ wavelength to characterize the nature of hydrated materials on Ceres. Absolute flux calibrations were made using observations of A0V stars at nearly the same elevations as each target. The Comet Siding Spring brightness in R-band was magnitude $R = 10.8$ in a photometric aperture of $17.4''$. The inferred H_2O production rate from Comet Siding Spring was $6 \times 10^{27} \text{ s}^{-1}$, assuming optically thin emissions, which may be a lower limit if optical depth effects are important. A superheat dust population was discovered at Comet Jacques, producing a bright infrared continuum without evidence for line emission. Observations of Ceres from BOPPS and from IRTF, obtained the same night, did not find evidence for a strong water vapor emission near $2.7 \mu\text{m}$ and led to an approximate upper limit $< 7 \times 10^{27} \text{ s}^{-1}$ for water emission from Ceres.

© 2016 Elsevier Inc. All rights reserved.

1. Introduction

The Balloon Observation Platform for Planetary Science (BOPPS) was a stratospheric balloon-borne payload developed as a system demonstration of a rapid response platform for time-critical planetary science opportunities. The BOPPS mission was a re-flight of the balloon payload developed for the BRRISON (Balloon Rapid Response for ISON) mission. This paper reports on BOPPS observations of two Oort Cloud comets, C/2013 A1 (Siding Spring) and C/2014 E2 (Jacques), and the dwarf planet 1 Ceres, as well as standard star observations for in-flight calibration.

Stratospheric balloon platforms can obtain new and high value planetary science (Kremic et al. 2013) by lifting a meter-class telescope, an instrument pointing system that achieves one arc second or better pointing stability, and instruments operating in the near-ultraviolet to mid-infrared wavelength range from 300 nm to 5000 nm, up to balloon altitudes of 35 to 40 km, above 99.5% of

the atmosphere. The BOPPS payload was a telescope of 80 cm aperture with a suite of imagers covering this wavelength range. At balloon altitudes, the atmospheric transmission and down-welling radiance permit observations of celestial bodies even within the fundamental atmospheric water absorption band at $2.7 \mu\text{m}$ and the $4.27 \mu\text{m}$ CO_2 absorption band. Moreover, the stratospheric balloon altitude is above practically all atmospheric seeing disturbances and the payload has access to space-like viewing conditions, with the potential to achieve diffraction-limited imaging at visible wavelengths from meter-class apertures.

In addition to observing from close to space, practically free from seeing, with observing windows through the atmosphere at wavelengths opaque to Earth-based observatories, balloon-borne platforms have several favorable attributes for planetary science. Some of these are: the potential for long duration observations (many weeks with super-pressure balloons), the possibility of observing some targets continuously without any diurnal limitation (e.g., over Antarctica), and the promise of achieving an annual mission cadence at low cost compared to space and airborne missions, with a potential for rapid response to emergent science opportunities. Balloon payloads can be recovered after flight and reused,

* Corresponding author.

E-mail address: andrew.cheng@jhuapl.edu (A.F. Cheng).

and they can be upgraded quickly. The rapid response, recovery, and successful re-flight were demonstrated on BRRISON and BOPPS (Adams et al. 2015; Cheng et al. 2015; Cheng 2015; Hibbitts et al. 2015).

This paper reports scientific findings from first light in the stratosphere for the BOPPS balloon observatory. The main objective of BOPPS was to observe an Oort Cloud Comet, C/2013 Siding Spring, shortly before its extraordinary close encounter with Mars which was observed by a fleet of spacecraft at Mars and at Earth. Comet Siding Spring passed within 100,000 km of Mars on Oct 19, 2014; BOPPS observed the comet on Sept. 26, 2014, when the comet was 114 million km from Mars.

The Oort Cloud is a distant repository of icy bodies, located approximately 10,000 to 50,000 AU from the Sun, that are little changed since the early solar system. Compositional studies of Oort Cloud comets, when they fortuitously visit the inner solar system, provide important opportunities to address how these comets formed. Oort Cloud comets are believed to have formed in the giant planet region, within ~ 15 – 20 AU, and to have been ejected into the distant repository by gravitational interactions with giant planets, mainly Neptune and Uranus, during an early epoch of planetary dynamical instability with migration of the four giant planets (Gomes et al. 2005; Morbidelli et al. 2005; Tsiganis et al. 2005).

The Oort Cloud is the more distant of the two major comet reservoirs in the solar system, the closer reservoir being the Kuiper Belt. An important question is whether comets in these reservoirs originated in different regions and formed from icy grains of different compositions. The comets in both of these reservoirs may have originated in the same primordial trans-Neptunian disk population and may share the same composition (Brasser and Morbidelli, 2013). There may also be an important contribution to the Oort Cloud from comets captured from other stars (Levison et al., 2010), possibly leading to distinct compositions. The ratio of H_2O to CO_2 in the comet may be an important diagnostic of cometary formation scenarios (Mumma and Charnley 2011; A'Hearn et al. 2013). Study of major volatiles in comets, meaning the main oxygen-bearing species H_2O , CO_2 , and CO , is also important for understanding the chemical environment of the solar nebula and interpreting the linkages between ices observed both in cometary nuclei and in the interstellar medium.

The importance of CO_2 as a driver of cometary activity even compared to water, within the inner solar system, was dramatically confirmed by Deep Impact at comet Hartley 2, where both water-rich and CO_2 -rich jets were observed (A'Hearn et al. 2011). Primary volatiles in addition to water are important in many comets, a key finding of the AKARI space-based infrared spectroscopic survey (Ootsubo et al. 2012) of 18 comets, which included 7 Oort Cloud comets. The AKARI mission measured H_2O , CO_2 , and CO emission rates in the 2.5– $5.0\ \mu\text{m}$ wavelength range during 2008–2010. Both H_2O and CO_2 were measured in 17 comets, with the $\text{CO}_2/\text{H}_2\text{O}$ ratio in cometary ice inferred to be $\sim 5\%$ to $\sim 30\%$ among comets observed at < 2.5 AU. The CO emission rate was measured in 3 comets, with upper limits obtained in the other 15 comets, finding that CO/CO_2 appears to be less than unity. The AKARI results led to a paradigm shift regarding the prominent role of CO_2 among cometary ices. Other measures of C abundances in comets c.f. (Bockelee-Morvan et al. 2004) have demonstrated a $\text{CO}/\text{H}_2\text{O}$ abundance ratio varying by 3 orders of magnitude between comets, while the $\text{CO}_2/\text{H}_2\text{O}$ abundance ratios are much more similar among comets, suggesting that CO_2 is the fundamental primitive carbon-bearing molecule in comets, and likely in the early solar system.

The BOPPS 2014 flight observed two Oort Cloud comets in addition to the seven observed by AKARI in the same 2.5 to $5.0\ \mu\text{m}$ wavelength range. BOPPS measured the H_2O and CO_2 emission rates with filter photometry, with the goal of measuring the $\text{CO}_2/\text{H}_2\text{O}$ ratio. BOPPS did not include filters to measure CO . During

its 19 h flight, BOPPS observed the two comets, C/2013 A1 (Siding Spring) and C/2014 E2 (Jacques), with the BIRC infrared multispectral imager. BIRC measured comet coma H_2O and CO_2 emissions at 2.7 and $4.27\ \mu\text{m}$, respectively, as a vital diagnostic of cometary origins.

BOPPS also observed the dwarf planet 1 Ceres using BIRC. Ceres has recently been reported to be a transient source of water vapor from localized regions on its surface, based on Herschel space-based sub-mm observations (Kueppers et al. 2014). Ceres is known to have hydrated minerals on its surface (DeSanctis et al. 2015; Rivkin et al. 2006; Vernazza et al. 2005). The BOPPS 2014 flight observed Ceres (Hibbitts et al. 2015) at the $2.7\ \mu\text{m}$ wavelength of water vapor emission, which wavelength also lies within the hydrated mineral absorption band around $3\ \mu\text{m}$.

With BIRC, BOPPS also characterized the down-welling sky radiance in the near-infrared at balloon altitudes, an important contributor to observed background signals. This sky radiance is the dominant contribution to background during the day and in the visible, but thermal emission backgrounds from the telescope and instrument are dominant at night and at long wavelengths. With the UVVis visible imager, BOPPS demonstrated sub-arc second pointing. UVVis consisted of two cameras covering the wavelength range from 0.3 to $0.85\ \mu\text{m}$, and its fine-steering mirror for tip-tilt corrections at 100 Hz was successfully demonstrated in flight. Although UVVis included filters to measure 309 nm OH emission, UVVis was operated to make stellar observations only during BOPPS and was not used to observe comets or Ceres (Kremic et al. 2015). This paper will present BIRC results from the BOPPS flight.

The BOPPS stratospheric balloon platform is shown in Fig. 1. About 6.7 m tall, it weighed 2296 kg including ballast for the BOPPS flight. The 19 h BOPPS flight on Sept. 25–26, 2014 reached a float altitude of 40 km. It accommodated an 0.8 m aperture telescope and separate optical benches for the two instruments, the BOPPS Infrared Camera (BIRC) and the Ultraviolet/Visible (UVVis) camera system. The balloon gondola and payload were recovered successfully after the BOPPS flight.

BIRC was a multispectral near infrared imager (McMichael et al. 2014) designed to observe one or more comets at wavelengths between 2.5 and $5\ \mu\text{m}$, with the Oort Cloud Comet, C/2013 A1 (Siding Spring), being of special interest. BIRC was originally developed rapidly, within 8 months, for BRRISON and was flown without modification on BOPPS. To meet the rapid schedule, BOPPS used an existing 0.8 m telescope, which was an $f/17.5$ Ritchey-Chretien with a 3 arc minute field-of-view (FOV). BIRC used a commercial camera procured from Teledyne Imaging Sensors, with a 4 Mpx HgCdTe detector and integrated cryocooler (see Fig. 1). This camera was modified to accommodate refocusing optics and a filter wheel. The principal BIRC characteristics are summarized in Table 1 and the optical design is shown in Fig. 2. The BIRC filter positions are shown in Fig. 3.

The Appendix gives additional technical details on the BOPPS mission in section A.1. Section A.2 describes the BIRC instrument, the instrument operations and image acquisition, and the image processing. Section A.3 describes ground test and calibrations. Sections A.4 and A.5 describe radiometric calibrations using a photon transfer test.

2. BOPPS flight observations

The BOPPS launch on the morning of Sept. 25 was delayed for over an hour by unfavorable ground-level winds, which eventually subsided to permit a successful launch at 08:20 (14:20 UTC). Although planned observation targets included Vesta and comet C/2012K1 PanSTARRS, with separate calibration star observations for each, the launch delay, followed by time required for com-

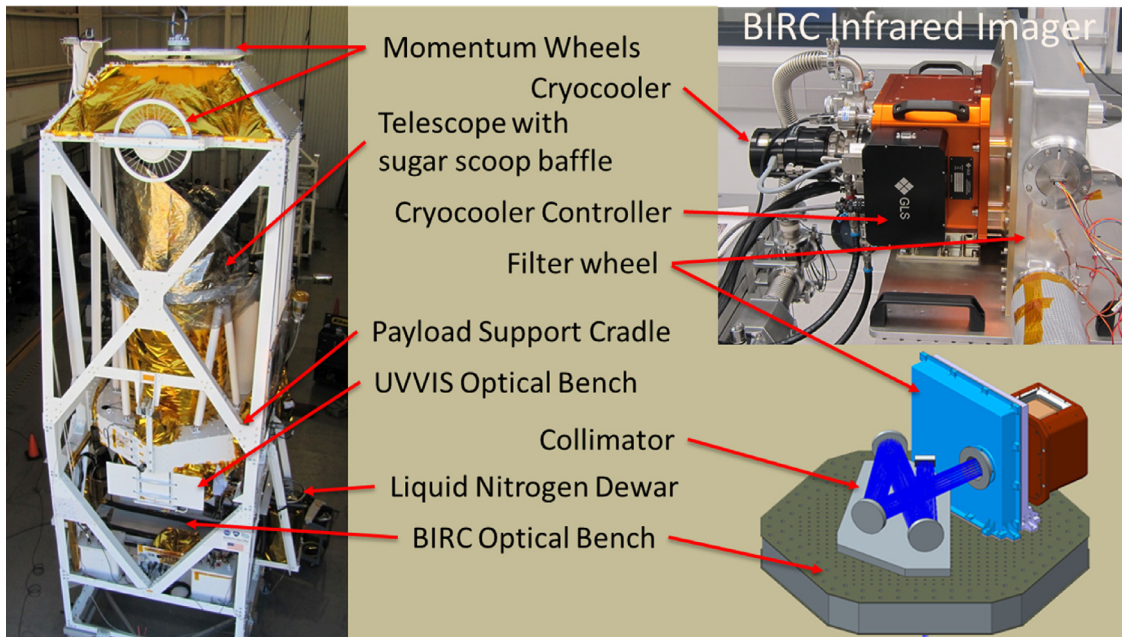


Fig. 1. (left) the BRRISON and BOPPS balloon gondola with 0.8 m telescope. The insets at right show (upper right) the BIRC infrared imager and (lower right) the BIRC optical bench, with collimator (cold enclosure removed), filter wheel and camera body. The total height of the BOPPS gondola was 6.7 m, and the total mass with LN2 and ballast was 2296 kg.

Table 1
BIRC Characteristics.

Main telescope optics	80 cm aperture diameter, $f/17.5$
FOV	3 arc minute
IFOV	plate scale 1.16 arc second per pixel
H2RG detector	2048 × 2048 HgCdTe detector; 5.1 μm long wavelength cutoff and 18 μm pixel pitch
Read noise	1.52 ± 0.065 DN
Frame rate and ADC	25 Mpx/s readout of 320 × 200 pixel images at 12 bit per pixel, minimum exposure 3.48 msec
Frame readout window	320 × 200 pixel image format; illuminated circle on detector, 155 pixel diameter
Filters	R band (~600 nm to ~800 nm); eight infrared filters centered at 2.47 μm , 2.70 μm , 2.85 μm , 3.05 μm , 3.20 μm , 4.00 μm , 4.27 μm , and 4.60 μm
Filter specifications	Infrared filter FWHM at 3% of center wavelength Infrared filter peak transmission > 80%, blocking 0.5–5 μm average < 0.01%, absolute < 0.1%

Table 2
Summary of BIRC Observations in BOPPS 2014 Flight.

Target	r_h [AU]	Δ [AU]	Phase [deg.]	Elevation [deg.] (Airmass)	Observation time [UTC]	Target Detections [band center μm]	Calibration star (type) mag	Calibration Star Elevation [deg]	Calibration Star Observation [UTC]
Siding Spring C/2013 A1	1.462	1.119	43	10.1 (AM = 5.5)	9-26-2014 00:20:31	R, 2.7, 2.47, 4.0	HD163761 (A0V) V = 6.69	6.3	9-26-2014 01:55:50
1 Ceres	2.747	3.3716	15	3.8 (AM = 12)	9-26-2014 02:40:51	R, 2.7, 2.47, 3.05, 3.2	HD133772 (A0V) V = 7.47	1.7	9-26-2014 03:00:50
Jacques C/2014 E2	1.716	1.146	34	57.1 (AM = 1.2)	9-26-2014 03:48:12	R, 2.7, 2.47, 3.05, 3.2, 2.85, 4.0, 4.27, 4.6	HD196724 (A0V) V = 4.82	63.2	9-26-2014 05:02:02

Notes: Sunset between Siding Spring and HD163761 calibration star observations; depletion of cryogen between Jacques and HD196724 observations, see text.

missioning and calibrating the guidance system for target acquisition, led to cancellation of these observations. These observations were planned for mid-day at solar elongations of 52.1° for Vesta and 52.5° for PanSTARRS, in which conditions the guidance system would not have obtained reliable star fixes.

Successful BIRC observations from the BOPPS flight are summarized in Table 2. For each target, Table 1 also shows the target heliocentric distance r_h , Earth distance Δ , and solar phase angle (Sun-target-observer angle), and the calibration star identity, spectral type and visual magnitude. The observation start times for each target and its calibration star are also shown, together with (apparent) elevation angles above horizontal. The horizon at a balloon float altitude of 40 km is at -6.4° elevation. Ephemeris data

were obtained from Horizons, and star data were obtained from SIMBAD (Wenger et al. 2000). The adopted absolute fluxes for the calibration stars are shown in Table 3.

The BOPPS flight observations plan allocated a separate calibration star for each target, with the calibration star chosen to match the elevation angle of the target observation to the extent possible. All calibration stars were of spectral type A0V, which lacks spectral features in the 2.5–5 μm wavelength range. The observing plan allocated equal times for calibration star observing and target observing, because of the need to obtain in-flight calibrations for BIRC which saw first light in the stratosphere during the BOPPS flight. None of the BOPPS filters has been used previously to observe any targets.

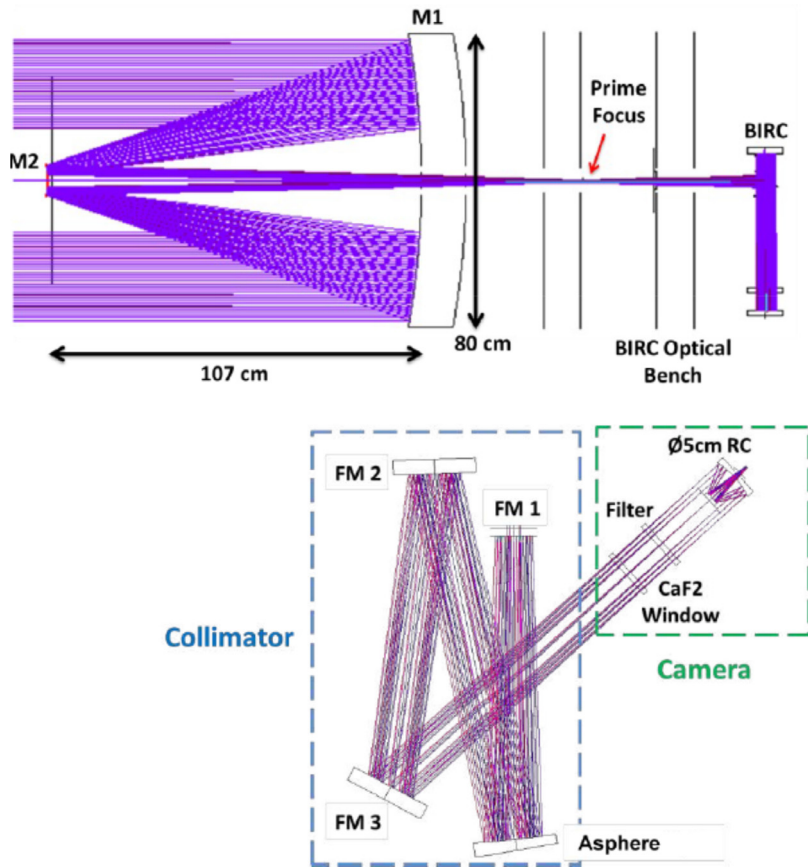


Fig. 2. Ray-trace cross-section schematic drawings of the BOPPS 0.8 m telescope, BIRC optical bench and BIRC camera. M1 and M2 are the primary and secondary mirrors of the 0.8 m telescope, respectively, with prime focus indicated at the UVVis optical bench. After passing through prime focus, light is folded into the plane of the BIRC optical bench at FM1 and collimated by an asphere. After two more fold mirrors, light passes into the camera and through the filter wheel, and it is focused onto the detector by RC, a 5 cm Ritchey–Chretien within the camera body.

Table 3
Calibration stars, absolute fluxes.

Filter	THz	HD163761 (for Siding Spring) flux [Jy], magnitude from SIMBAD	HD196724 (for Jacques) flux [Jy], magnitude from SIMBAD	HD133772 (for Ceres) flux [Jy], magnitude from SIMBAD
SDSS u'	851.9		23.9Jy	
Johnson B	674.9	9.4 Jy, B = 6.68	B = 4.8	4.1 Jy, B = 7.55
Johnson V	541.4	7.9 Jy, V = 6.69	43 Jy, V = 4.82	3.7 Jy, V = 7.47
HIP BT	713.3		49.2Jy	
HIP VT	563.6		45.6Jy	3.8Jy
SDSS r'	479.9	6.8Jy	39.3Jy	3.3Jy
SDSS i'	392.7	5.6Jy	31.4Jy	2.9Jy
SDSS z'	332.4	4.9Jy	27.5Jy	2.6Jy
2MASS J	242	3.3 Jy, J = 6.691	13.7 Jy, J = 5.153	2 Jy, J = 7.242
2MASS H	181.8	2 Jy, H = 6.772	11.3 Jy, H = 4.924	1.4 Jy, H = 7.225
2MASS K	138.6	1.3 Jy, K = 6.746	7.6 Jy, K = 4.85	0.847 Jy, K = 7.238
WISE W1	89.5	0.643Jy	3.5Jy	0.398Jy
WISE W2	65.2	0.344Jy	2.5Jy	0.218Jy
R	467.9	Adopted 6.46Jy	Adopted 37.19Jy, R = 4.79	Adopted 3.21Jy
BIRC 2.47 μ m	121.4	Adopted 1.014Jy	Adopted 6.83Jy	Adopted 0.65Jy
BIRC 2.70 μ m	111.0	Adopted 0.867Jy	Adopted 5.87Jy	Adopted 0.559Jy
BIRC 2.85 μ m	105.2		Adopted 5.34Jy	
BIRC 3.05 μ m	98.29	Adopted 0.697Jy	Adopted 4.745Jy	Adopted 0.453Jy
BIRC 3.2 μ m	93.69	Adopted 0.639Jy	Adopted 4.36Jy	Adopted 0.416Jy
BIRC 4.0 μ m	74.95		Adopted 2.92Jy	
BIRC 4.27 μ m	70.21		Adopted 2.595Jy	
BIRC 4.6 μ m	65.17		Adopted 2.26Jy	

Adopted fluxes from interpolation of fluxes [Jy] with Planck function, see text

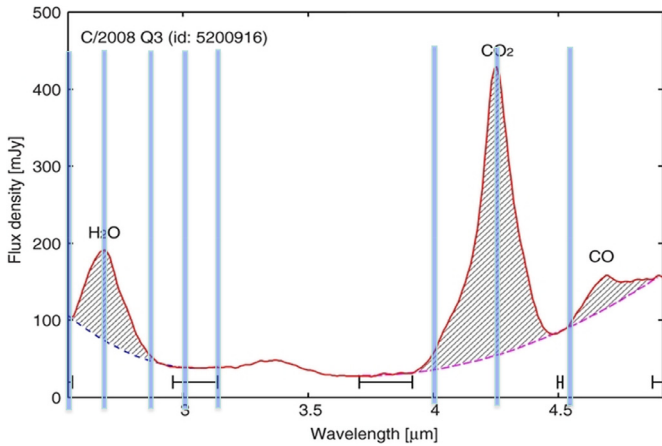


Fig. 3. BIRC infrared filter positions (blue bars), plotted on AKARI spectrum of comet C/2008Q3 Garradd (Ootsubo et al. 2012). The BIRC filter wheel also accommodated an R filter, not shown.

The observed count rate DN/s from a target is comprised of

$$\begin{aligned} \text{Observed signal} = & (\text{Source signal}) * \text{extinction} \\ & + \text{sky background} + \text{instrument background} \end{aligned} \quad (1)$$

The sky and instrument backgrounds are removed by aperture photometry, where the count rate is determined within a series of successively larger apertures on the sky, so as to find the background level to subtract from the source count rate in the selected aperture. The sky and instrument backgrounds are not separated by aperture photometry, but consideration of the backgrounds in different filters, with independent knowledge of the spectrum of the sky background, allows inferences to be drawn about the sky and instrument backgrounds separately.

The atmospheric extinction at the observed wavelengths was not measured directly, but was accounted for by choosing a calibration star for each target at almost the same elevation angle (and azimuth angle, both within typically a few degrees), so that the extinctions are assumed to be the same for calibration star and for target.

The BOPPS estimate of absolute fluxes from the targets was obtained essentially from a ratio spectrum, of each target to its individual calibration star, adopting absolute fluxes at each BOPPS filter wavelength for the calibration star and comparing observed count rates in each observed filter between target and calibration star. The photon transfer characteristic, relating DN/s to detected photoelectrons/s, was that found from radiometric calibration (Appendix A.3, Eq. 6). In other words, we write

$$\begin{aligned} \text{Detected } e^-/s = & (\text{incident photon/s AMO}) \\ & * (\text{system detection efficiency}) * \text{extinction} \end{aligned} \quad (2)$$

The observed DN/s from the calibration star is used to find the detected photoelectrons/s, after which the known incident flux at the top of the atmosphere is used to find the product of system detection efficiency and (atmospheric) extinction. The same product of system detection efficiency and extinction is then used to find the target incident flux from its observed DN/s. The system detection efficiency here involves the system optical transfer efficiency from main telescope through collimating and re-focusing optics, the filter transmission characteristics and pass bands, the source spectra, and detector quantum efficiency. These contributions were not determined or measured separately, but since the

BOPPS payload was recovered in excellent condition, further characterization is possible in future work.

This procedure to estimate the absolute fluxes involves numerous simplifications to meet budget and schedule. To begin with, the differential extinction between calibration stars and corresponding targets, as well as differences between the AOV star spectra and target spectra, are not accounted for, but a more important simplification arises from the adopted calibration star fluxes. The calibration star fluxes are reported in JHK filters and at filter wavelengths measured by WISE, but not at the filter wavelengths measured by BOPPS. The adopted calibration star fluxes used for BIRC radiometry are interpolated to the BIRC filter wavelengths, using a Planck function fitted to the reported calibration star fluxes. This interpolation was compared to a simple power law interpolation using JHK and the WISE W1 and W2 filter fluxes (at 3.35 and 4.6 μm respectively), finding that the two interpolations agreed within $\sim 5\%$.

Table 3 shows the reported values of the calibration star fluxes as given by the SIMBAD and Vizier databases (Wenger et al. 2000), together with the adopted flux values from interpolation to the center wavelengths of the BIRC filters. Individual entries in Table 3 also give the filter magnitude if listed by SIMBAD.

3. Results and discussion

The results of aperture photometry for Siding Spring, Jacques, and Ceres and for their respective calibration stars are given in Tables 4–6 respectively. The tables show mean count rates in DN/s and the standard deviations that were determined from the scatter of individual measurements, where the complete observation of a given target or calibration star was subdivided into multiple, non-overlapping segments and shifted, co-added and processed independently in each segment.

All observations, except for the Siding Spring calibration star HD163761, were obtained in two sets, with a gondola pointing offset between the two sets, and with each set cycling through all observed filters. For HD163761, time pressure did not permit acquisition of the second set. For the targets observed with two sets, the target is in a different location in the FOV for the second set compared with the first. Each set was used to obtain the flatfield for images of the other set, without removing the target. Thus if the first set produced the flatfield, the processed images of the second set have a “negative image” of the target at the target location in the first set. This negative image is well separated from the desired target image and is ignored for aperture photometry. For HD163761 the flatfield was obtained from the Ceres image set B. Flatfields from ground test were found not to be useful owing to very different environmental conditions encountered in flight.

Flatfields were generated by collating bias-subtracted images from a given observation in a given filter (separate flatfields generated for every filter). Spatial and temporal median filtering was applied to remove pixel-to-pixel noise. The filtered images are then co-added, divided by the number of images co-added, and normalized using the mean value of the averaged image in the 3 arcmin field of view. An example of a shifted, co-added, filtered and flatfielded image is shown in Fig. 10. This image also illustrates digital noise from misaligned skew, which was recognized shortly afterwards in real-time downlinked images and corrected in-flight.

Table 4 shows the count rates from Comet Siding Spring and its calibration star HD163761, in e^-/s , from aperture photometry with a circular aperture of 15 px diameter (177 pixels, 17.4 arc sec diameter). Also shown are the standard deviations from subdividing the dataset and the total exposure times (in this case, 59.2 s in each filter). Finally, the table shows the background levels in $e^-/s/\text{px}$, which arise from a combination of sky emissions and instrument backgrounds. There was a notable decrease in the background be-

Table 4
Comet Siding Spring and calibration star.

Filter	HD163761 e-/s	s.d. (%)	time (s)	HD163761 bkgd e-/s/px	Siding Spr. e-/s	s.d. (%)	time (s)	Siding Spr. bkgd e-/s/px
R	1.686E+06	0.55%	59.2	3.780E+03	3.736E+04	12.5%	59.2	2.167E+05
BIRC 2.47 μm	7.896E+04	3.93%	59.2	5.747E+03	1.801E+04	10.3%	59.2	7.0239E+03
BIRC 2.70 μm	6.876E+04	0.77%	59.2	8.086E+03	2.107E+04	5.6%	59.2	1.3261E+04
BIRC 2.85 μm								
BIRC 3.05 μm	9.331E+04	4.19%	59.2	1.196E+05				
BIRC 3.2 μm	8.968E+04	7.75%	59.2	1.328E+05				
BIRC 4.0 μm								
BIRC 4.27 μm								
BIRC 4.6 μm								

Table 5
Comet Jacques and calibration star.

Filter	HD196724 e-/s	s.d. (%)	time (s)	HD196724 bkgd e-/s/px	Jacques e-/s	s.d. (%)	time (s)	Jacques bkgd e-/s/px
R	1.163E+07	1.3%	27.1	3.041E+04	1.279E+04			2.201E+03
BIRC 2.47 μm	5.257E+05	0.9%	27.1	2.978E+04	5.319E+04	2.2%	118.4	3.4923E+03
BIRC 2.70 μm	5.004E+05	1.9%	27.1	3.113E+04	5.731E+04	3.7%	118.4	4.3667E+03
BIRC 2.85 μm	4.759E+05	5.3%	27.1	2.222E+05				
BIRC 3.05 μm	5.219E+05	3.5%	27.1	9.511E+04	5.141E+04	4.3%	93.8	7.0915E+04
BIRC 3.2 μm	4.411E+05	9.0%	27.1	9.800E+04	7.384E+04	8.7%	118.4	8.0110E+04
BIRC 4.0 μm	1.740E+05	14.8%	119.9	2.939E+05	5.008E+04	17.8%	413.5	2.693E+05
BIRC 4.27 μm	1.740E+05	22.0%	107.9	1.409E+06	6.943E+04	3.3%	59.1	1.434E+06
BIRC 4.6 μm	3.833E+05	18.4%	27.1	1.844E+06				

Table 6
Ceres and calibration star.

Filter	HD133772 e-/s	s.d. (%)	time (s)	HD133772 bkgd e-/s/px	Ceres e-/s	s.d. (%)	time (s)	Ceres bkgd e-/s/px
R	6.925E+05	15.1%	118.4	3.544E+03	4.961E+05	4.4%	118.4	3.590E+03
BIRC 2.47 μm	4.680E+04	5.4%	118.4	5.030E+03	3.936E+04	3.7%	118.4	5.246E+03
BIRC 2.70 μm	3.540E+04	16.4%	118.4	6.395E+03	3.094E+04	13.8%	118.4	6.845E+03
BIRC 2.85 μm								
BIRC 3.05 μm	4.627E+04		59.2	9.315E+04	3.336E+04	10.0%	118.4	9.918E+04
BIRC 3.2 μm	4.000E+04	34.5%	79	9.901E+04	3.437E+04	9.3%	118.4	1.067E+05
BIRC 4.0 μm								
BIRC 4.27 μm								
BIRC 4.6 μm								

tween the Siding Spring observation and the HD163761 observation, particularly in R band, because the Sun set between these observations. No observations were made of Comet Siding Spring or its calibration star HD163761 in the 4.27 μm CO₂ filter owing to insufficient remaining time before Ceres observations needed to start.

Table 5 shows the same information as Table 4, for the Comet Jacques and HD196724 observations. The same aperture was used for aperture photometry. Count rates in all 9 BIRC filters are shown for HD196724, including the 2.85 μm filter which was not used for any other observation, because of excessive out-of-band response seen in ground test. The anomalously high background rate seen in this filter is also evidence of out-of-band response. The observations of HD196724 were the last observations of the flight for BIRC (UVVis observations followed), and the LN₂ cryogen was depleted, leading to a gradual loss of thermal control. The background rates are significantly elevated in all of the short wavelength filters (R, 2.47 and 2.7 μm) for the final observations of HD196724 compared to those of Siding Spring in Table 4.

Table 6 shows the results for Ceres and its calibration star HD133772, again with the same photometric aperture. The observations of HD133772 were cut short because the star set, accounting for the reduced observation times in the 3.05 and 3.2 μm filters. Ceres was observed at very high airmass of 12 or more, but the background level even at 2.7 μm is only modestly greater than that for Jacques at airmass 1.2, by a factor 1.6.

Fig. 4 shows the measured fluxes from comets Siding Spring and Jacques and from Ceres, with their respective calibration stars. Each target spectrum is a measured ratio to the adopted calibration star spectrum. The inferred system detection efficiencies are consistent with each other and with those from ground testing, but because of the varying conditions during the flight (day versus night, temperature changes), the radiometric calibration procedure was implemented separately for each target.

Although Comet Jacques (Fig. 4b) is about 0.3 times as bright as Siding Spring (Fig. 4a) in R band, it is about four times brighter at 2.47 μm where the emitted flux is 0.69 Jy. The emitted flux from Jacques generally increases with wavelength, to 1.0 Jy at 4.27 μm , without a clear indication of line emission. This bright near-IR emission is interpreted as a superheated infrared continuum, like that observed in many hyperbolic or long period comets (Gehrz and Ney 1992; Hanner et al. 1997). Superheat indicates a population of hot dust particles large enough compared to infrared wavelengths to be inefficient thermal emitters, so that they are raised to well above the blackbody equilibrium temperature at the comet's distance from the Sun.

We have fitted a model for the superheat dust thermal emission from Comet Jacques, where the Planck function is multiplied by a power law correction factor of the form $(\lambda/1.5 \mu\text{m})^{-2.2}$ to account for inefficient thermal emission (Lisse et al. 1998). The superheat model is approximately consistent with the continuum fluxes in Fig. 4b, for an assumed temperature of 500 K, an emissivity 0.9, a phase correction of 0.34 magnitudes, and a superheat (large par-

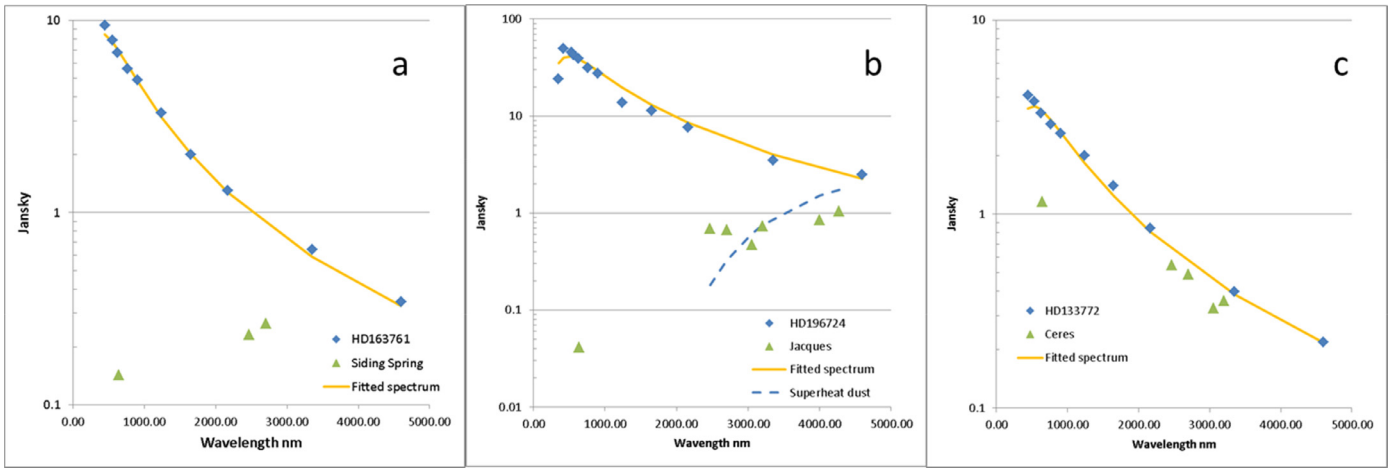


Fig. 4. BOPPS measured fluxes of (a) Siding Spring, (b) Jacques, and (c) Ceres. Diamonds show reported fluxes of calibration stars with fitted Planck functions (solid curves) that were used for absolute flux calibration. BOPPS measured fluxes shown with triangles in all three panels. Superheat dust model plotted in panel (b), dashed curve.

ticle) emitting area 1400 km^2 . This dust area is reasonable in the light of the $Af\rho = 9 \text{ m}$ for Jacques. The quantity $Af\rho$ measures the amount of dust scattering (A'Hearn et al. 1984), and for an average albedo of 0.05, the total dust scattering area is 4100 km^2 , exceeding the area in superheated particles. This is a plausible result, as superheats arise from small, sub-micron amorphous carbon particles which account for about 10–90 % of all dust particles in comets (Lisse et al. 1998, 2007; Kelley and Wooden 2009).

The Comet Siding Spring R magnitude observed by BOPPS was $R = 10.8$, leading to $Af\rho = 22 \text{ m}$. The water production rate $Q(\text{H}_2\text{O})$ was estimated from the flux difference $\text{flux}(2.7\mu\text{m}) - 0.75 \cdot \text{flux}(2.47\mu\text{m})$ in order to take account of the continuum slope (Yang et al. 2009). The average column density N of molecules within the $17.4''$ photometric aperture of diameter d is written $N = \frac{Q}{vd}$ where v is gas outflow velocity (Bocklee-Morvan et al. 2004). The photometric aperture diameter is $14,130 \text{ km}$, at Earth distance $\Delta = 1.119 \text{ AU} = 1.674 \times 10^8 \text{ km}$. The photometric aperture is much less than the distance traveled by the molecule over its photo-dissociation lifetime. Then the flux $(2.7\mu\text{m}) = Qgd/(16v\Delta^2)$ photons $\text{m}^{-2} \text{ s}^{-1}$ and the water production rate is

$$Q(\text{H}_2\text{O}) = \frac{(16Fv\Delta^2)}{gd} = (6 \pm 30\%) \times 10^{27} \text{ s}^{-1} \quad (3)$$

assuming $v = 800 r_H^{-0.5} = 660 \text{ m/s}$ at $r_H = 1.462 \text{ AU}$, and using water band g-factors from (Bocklee-Morvan and Crovisier 1989). This estimate and the stated uncertainty assume optically thin conditions. A more complete treatment considering optical depth effects is deferred to a subsequent paper. Significant optical depth of the emitting region would increase the water production rate estimated from the observed $2.7 \mu\text{m}$ flux, and this effect is not included in the uncertainty.

The Comet Siding Spring water production rate from BOPPS can be compared to that inferred from a statistical correlation with V magnitude (Jorda et al. 2008) derived from 234 observations of 37 comets. The BOPPS observed $R = 10.8$ is converted to V magnitude assuming solar color $V - R = 0.41$ and reduced to 1 AU distance, yielding the heliocentric magnitude $m_H = 11.0$, for which the (Jorda et al. 2008) correlation predicts $Q(\text{H}_2\text{O}) = 9.7 \times 10^{27} \text{ s}^{-1}$. The BOPPS production rate is a factor 1.6 below the correlation prediction, which would put Siding Spring within the scatter of the 37 comets regarding water production rate relative to heliocentric magnitude. However, the BOPPS water production rate may be underestimated because of optical depth effects.

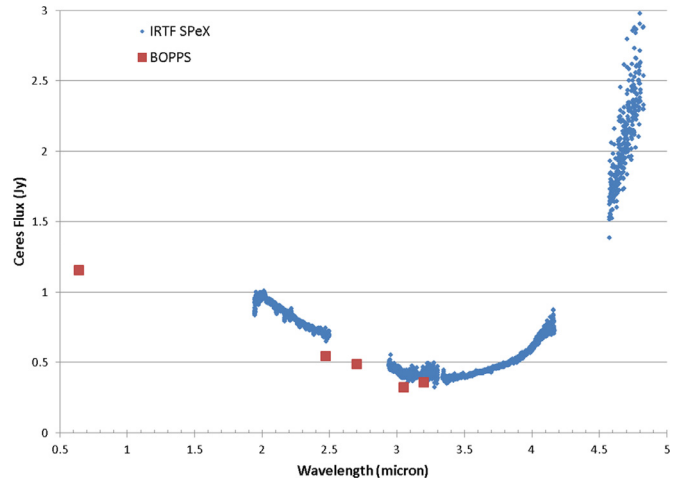


Fig. 5. BOPPS measured fluxes of Ceres compared to fluxes measured by NASA/IRTF on September 25, 2014.

Comet Siding Spring was observed by *Swift* (Bodewits et al. 2015) with visible filter measurements of OH emission on several dates from Jul. 9 through Oct. 23, around the comet's closest approach to Mars on Oct. 19. *Swift* found water production rates ranging from 1.1×10^{28} to $1.7 \times 10^{28} \text{ s}^{-1}$. (Crismani et al. 2015) observed H Lyman- α with MAVEN IUVS on October 14 and 18 and found similar values around $1.1 \times 10^{28} \text{ s}^{-1}$. These observed water production rates are factors of 2 to 3 higher than the BOPPS value suggesting that the BOPPS value may be low because of optical depth effects. (Bodewits et al. 2015) did measure a lower value of $2.4 \times 10^{27} \text{ s}^{-1}$, similar to the BOPPS value, on May 29 at $r_h = 2.46 \text{ AU}$; they attributed the sudden increase in water production after May 29 to increased sublimation of icy grains in the coma. It is cautioned that the BOPPS observations used much smaller photometric apertures than the *Swift* observations, and moreover the BOPPS observations occurred 8 days after and 17 days before the closest *Swift* observations.

Fig. 5 shows the BOPPS fluxes measured from Ceres compared to the measured spectrum of Ceres obtained the same night from the NASA/IRTF 3 m telescope using the SpeX 0.8 – 5.0 μm spectrometer in low resolution, high throughput mode. There is good agreement as to spectral shape with the BOPPS spectrum only $\sim 20\%$ lower in absolute flux calibration. The BOPPS observations at $2.7 \mu\text{m}$, a wavelength which cannot be measured at IRTF, did not

provide strong evidence for water vapor emission at 2.7 μm from Ceres. Observations of Comets Siding Spring and Jacques were also obtained from the IRTF during the BOPPS flight, but yielded poor quality data, not reproduced here.

Comparison of BOPPS and IRTF Ceres flux measurements suggests an average absolute flux calibration uncertainty of $\pm 20\%$ from the use of calibration stars as in Table 3. Combined with the uncertainties shown in Table 4, we estimate $\pm 30\%$ uncertainty in the continuum-removed 2.7 μm flux used for (3).

The solid body reflectance spectrum from Ceres exhibits a spectral absorption feature about 10% deep at 3.05 μm (DeSanctis et al. 2015; Vernazza et al. 2005; Rivkin et al. 2006). The BOPPS-observed fluxes from Ceres in Fig. 5 are such that the 2.7 μm flux falls close to a linear interpolation between the fluxes at 2.47 μm and 3.2 μm , consistent with the presence of the 3.05 μm absorption feature. BOPPS did not find evidence for water emission from Ceres. An approximate upper limit to the emission rate is obtained from the excess of 2.7 μm flux above the linear interpolation between the 2.47 μm flux and 1.1 times the 3.05 μm flux (to account for the spectral absorption there), yielding a water source $< 7 \times 10^{27}$ molecules s^{-1} . The excess of 2.7 μm flux above the linear interpolation between the 2.47 μm flux and the 3.2 μm flux yields almost the same result. The localized transient water vapor emission from Ceres at $\sim 10^{26}$ molecules s^{-1} , as observed by Herschel (Kueppers et al. 2014), would not have been detected by BOPPS.

4. Conclusions

The potential of stratospheric balloon platforms for time-critical planetary science opportunities has been demonstrated by BRRISON and BOPPS. The September, 2014 BOPPS flight successfully observed the two Oort Cloud comets C/2013 Siding Spring and C/2014E2 Jacques. The Comet Siding Spring brightness in R-band was magnitude $R = 10.8$ in a photometric aperture of 17.4". The inferred H_2O production rate from Comet Siding Spring was $3 \times 10^{27} \text{ s}^{-1}$, assuming optically thin emissions, but comparisons with OH and H Lyman- α observations from *Swift* and MAVEN, respectively, suggest that this BOPPS water production is a lower limit presumably because of significant optical depth of the 2.7 μm emitting region. A superheat dust population was discovered at Comet Jacques. Observations of Ceres from BOPPS and from IRTF, obtained the same night, did not find evidence for any strong water vapor emission near 2.7 μm .

Acknowledgements

We are happy to acknowledge the critical support of the NASA Glenn Research Center. The success of the BOPPS mission was due to the hard work and dedication of engineering teams at APL and at SwRI, as well as NASA/CSBF, Nu-Tek, QED, SYDOR, Teledyne Imaging Systems, IR Labs, and GL Scientific. This work was funded by NASA under contract NNN06AA01C. We thank J. Rayner at the IRTF for his assistance. CML and MLS obtained data at IRTF for this work. IRTF is operated by the Univ. of Hawaii under contract with NASA.

Appendix

A.1. BOPPS mission overview

The BOPPS mission was a system development and demonstration of a rapid response balloon-borne scientific payload for a time-critical planetary science opportunity (Kremic et al. 2015). In February, 2013, NASA Glenn Research Center, the Johns Hopkins University Applied Physics Laboratory (JHU/APL), and the Southwest Research Institute (SwRI) were tasked by NASA to develop

the BRRISON mission to observe the sun-grazing Oort Cloud comet C/2012 S1 (ISON), that made a close approach to Earth in November, 2013. After a rapid, 8 month development, BRRISON was launched on Sept. 28, 2013 for a 12 h flight, reaching a float altitude of 130,000 ft (40 km). However, a flight anomaly occurred, and it did not observe ISON. The BRRISON payload was recovered successfully, and it was re-flown on the BOPPS mission a year later in September, 2014, from Fort Sumner, NM.

The BOPPS mission (Adams et al. 2015) was the second flight of the platform (Fig. 1), which launched from Ft. Sumner, NM, at 08:20 local time on September 25, 2014, and also ascended to 130,000 ft altitude. For BOPPS the platform weighed 2296 kg including ballast. The BOPPS instrument suite was the same as for BRRISON and consisted of the BOPPS IR Camera (BIRC), developed by APL, and the Ultraviolet/Visible (UVVis) camera system, developed by SwRI. The instruments were accommodated on separate optical benches behind the 0.8 m telescope. The balloon gondola and payload were recovered successfully after the BOPPS flight.

A.2. BIRC instrument

The BOPPS Infrared Camera (BIRC) was a multispectral infrared imager (McMichael et al. 2014) designed to observe one or more comets at wavelengths between 2.5 and 5 μm , with the Oort Cloud Comet, C/2013 A1 (Siding Spring), being of special interest. BIRC was originally developed rapidly, within 8 months, for BRRISON and was flown without modification on BOPPS. To meet the rapid schedule, BRRISON and BOPPS used an existing 0.8 m telescope, which was an $f/17.5$ Ritchey-Chretien with a 3 arc minute field-of-view (FOV). In addition, a commercial camera was procured from Teledyne Imaging Sensors, with a 4 Mpx HgCdTe H2RG detector system, an integrated Sunpower cryocooler, and SIDECAR ASIC cryogenic focal plane electronics with an external data acquisition interface card (see Fig. 1). This camera was modified to accommodate refocusing optics and a filter wheel for BIRC (see Table 1).

The BIRC optical design (Fig. 2) is a focal reducer, bringing the $f/17.5$ beam from the 0.8 m main telescope through a collimator and a filter wheel, and then re-focusing the light as a faster $f/4$ beam at the detector, while maintaining the full 3 arc minute FOV (McMichael et al. 2014). Fig. 2 shows ray trace cross sections of the main telescope and optical benches and of the collimating and re-focusing optics. The re-focusing is accomplished by a small, 5 cm aperture Ritchey-Chretien telescope mounted inside the camera body, within the camera's cryogenic vacuum system.

The BIRC optomechanical and thermal designs (McMichael et al. 2014) used a nitrogen-purged cold enclosure mounted on the BIRC optical bench, housing the collimator optics which consisted of a collimating asphere and three fold mirrors, all of which are coated with protected gold to reduce thermal self-emission. After passing through prime focus of the main telescope, light enters the cold enclosure through a CaF_2 window, and a collimated beam exits the cold box through another CaF_2 window. This second window closes off the cold enclosure on one side and the camera body vacuum system (at $< 1e-5$ Torr) on the other. The LN₂-cooled, nine-position filter wheel and the small Ritchey-Chretien telescope are both mounted inside the camera body vacuum system. During the BOPPS flight, the cold enclosure optics were maintained by nitrogen purge at ~ 150 K, while the filter wheel was cooled to ~ 110 K by LN₂, and the H2RG detector was operated at ~ 70 K. The primary and secondary mirrors of the main telescope were kept at ambient temperature to avoid condensation, although they were gold-coated. In addition, the first CaF_2 window, where light enters the cold enclosure, is the thermal interface to the UVVis optical bench which is maintained near $\sim 10^\circ\text{C}$. The primary and secondary mirrors of the 0.8 m

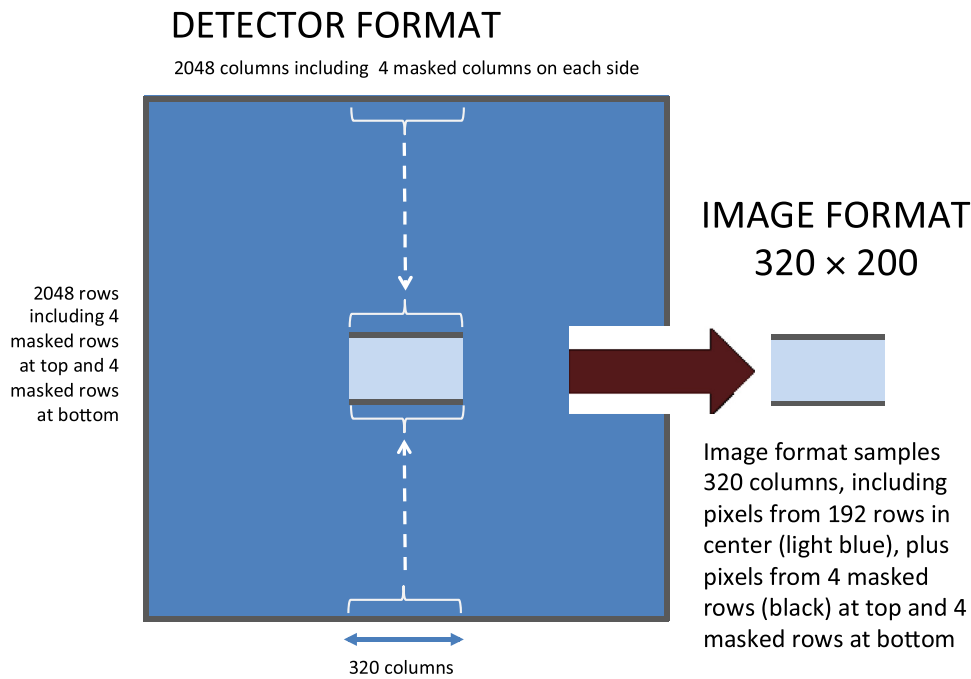


Fig. 6. BIRC image format of 320 columns by 200 rows. The windowed readout includes the illuminated portion of the detector (a circle of diameter 155 pixels at the center) as well as pixels from 4 masked rows at top and 4 masked rows at bottom.

telescope and the first CaF_2 window are the main sources of thermal background emission for BIRC.

The BIRC filter wheel accommodated 9 filters, a standard R filter and 8 infrared filters (see Table 1), with the infrared filter widths specified to be 3% of the center wavelength. The filter positions (see Fig. 3) were chosen to measure cometary water and CO_2 emissions at $2.7\ \mu\text{m}$ and $4.27\ \mu\text{m}$, respectively, with accompanying continuum measurements. The filter positions near $3\ \mu\text{m}$ were selected also bearing in mind the objective of characterizing the hydrated mineral absorption feature on asteroids or the Moon.

For BIRC the $3'$ illuminated FOV is centered on the detector. As this FOV is a circle of 155 pixel diameter on the detector, a windowed readout was implemented for BIRC flight data, producing images with a 320×200 pixel format (McMichael et al. 2014; also see Fig. 6) using custom firmware for the SIDECAR ASIC which controls and reads out the focal plane array. The data is sent parallel, double data rate at 80 MHz (160 Mword/sec) with LVDS signaling. Since the ASIC does not provide a return data clock to the external interface card, signal skew can occur on this long cable producing digital noise. The interface card provides a skew adjustment word to manage signal skew. An experimentally determined constant skew setting was used, with the SIDECAR operated at a precisely controlled temperature for bias and gain stability, limiting skew variability, with the skew setting adjusted as necessary. For the BOPPS flight data from Comet Jacques, the skew was adjusted in-flight.

The BIRC observations targeted faint objects against much brighter backgrounds from sky emission and instrument thermal emission. Hence short exposures are required, to avoid saturating on background, with co-addition of many exposures to accumulate sufficient signal photons. For BOPPS (McMichael et al. 2014), a fast mode readout was implemented for the SIDECAR/H2RG to enable rapid acquisition of short exposures. These data are digitized at 5 Mpx/sec with 12 bit resolution, in each of 5 ports used for the BIRC windowed readout. The minimum frame exposure time was 3.48 msec.

For BRRISON and BOPPS, the acquisition of targets for observations was accomplished manually using guide telescope images,

which were either images acquired by the star cameras or images acquired by BIRC (through the main telescope), returned to the ground in close to real time. A pointing error of only $1.5'$ would suffice to put the target outside the BIRC FOV. The lightweight main telescope was designed for use in zero gravity, and on BOPPS, it exhibited significant alignment shifts with orientation changes. Significant effort was expended to compensate for the pointing shifts with calibrations of the gondola guidance system, but the BOPPS flight experience was that after a large angle slew, the initial target acquisition process required manual adjustment of pointing with the assistance of guide telescope images.

Given that BIRC was required to observe faint targets against a very bright background, many BIRC images (hundreds to thousands) need to be co-added to detect a target with sufficient signal-to-noise ratio, quantified by the ratio of target e-/s to its background e-/s (from Tables 4–6) integrated over the $17.4''$ photometric aperture. To use BIRC images as guide telescope images, or to confirm that the desired target has been acquired by BIRC, ground pipeline image processing was developed for BIRC to shift and co-add images in close to real time at the field operation center. The amounts of image shift required to compensate for platform pointing jitter and drift were obtained from the gondola inertial measurement unit data, also downlinked in near real time to support image shifting and co-adding.

The image shifting and co-adding process consisted of two main steps. The first step removed pixel-to-pixel (high spatial frequency) noise in individual frames due to “hot” or “cold” pixels and random telegraph noise. The second step used the gondola pointing information from the inertial measurement unit to determine the magnitude and direction of the image shift required to maintain a fixed inertial pointing for each image pixel. For the first step, both spatial and temporal filters were applied to remove pixel-to-pixel noise. A spatial median filter was applied to each image to remove bad, or unresponsive, pixels, which were then replaced by the median value of a 3×3 pixel region centered on the bad pixel. Then a 10 image temporal sliding window was applied over the entire set of images. The sliding window evaluated a 3×3 region centered on each pixel location over 10 successive images in order to de-

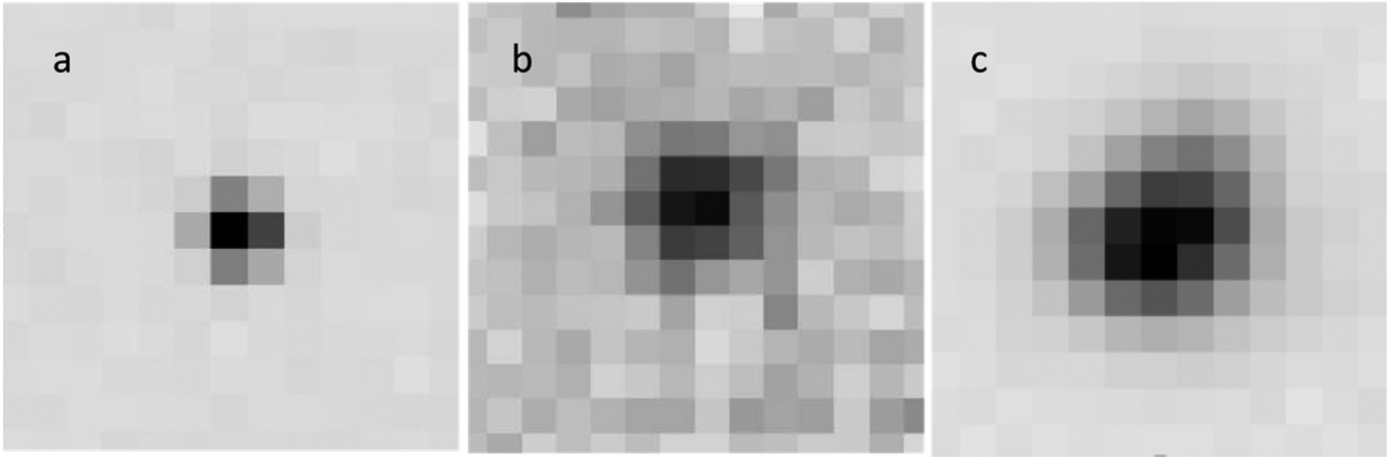


Fig. 7. Images of point sources from ground test. (a) the PSF of the camera assembly, with FWHM = 2 pixels across full FOV; (b) the PSF of the integrated collimator and camera assembly, with high rate nitrogen purge under laboratory ambient conditions, FWHM ~ 3.5 pixel; (c) the PSF of integrated system with main telescope, in hang test at Ft Sumner observing the star HD73598, showing PSF with FWHM ~ 4 pixel.

termine the mean and variance of the region over the time span in which the ten images were taken. Pixels more than 5-sigma off the mean in each region were excluded.

These de-spiked images were then interpolated by 5x to allow for sub-pixel shifting guided by pointing information, which consisted of the target right ascension and declination, the instantaneous angular shifts in elevation and azimuth required to point the telescope boresight to the target, and the time, captured at a rate of 20 Hz. This information was interpolated to calculate the row and column shifts for each image. This image motion compensation did not account for rotations of the telescope around its boresight. The software then calculated the row and column shifts with respect to the first image in the image set, determined the maximum values of these shifts, and created an image canvas large enough to accommodate the maximum shifts. The software then calculated an average stacked image from the shifted images, accounting for the number of images placing data at each row and column location (Fig. 12).

A.3. BIRC ground test and calibrations

The image quality was tested separately for the camera assembly, the collimator assembly, and the main telescope, after which it was also measured as an integrated system in ground test and in flight with star calibrations (McMichael et al. 2014). For the camera assembly alone, consisting of window, filter wheel, and RC re-focusing optics, the point spread function (PSF) measured across the full field of view in R band had a FWHM of 2 pixels (see Fig. 7a). After the collimator was assembled and integrated with the camera, the PSF imaged in the R band, with nitrogen purge and cryocooler operating, had PSF ~ 3.5 pixel (Fig. 7b) limited by ‘seeing’ within the collimator. After integration and alignment with the main telescope, the PSF was measured for the integrated optical system in a ‘hang test’, where the gondola is suspended from a crane, free to rotate, allowing the payload to observe the night sky. The system PSF in R band including gondola pointing, during the Sept. 21, 2013 hang test at Ft Sumner, had FWHM ~ 4 pixel (Fig. 7c).

BIRC radiometric calibrations were performed in ground test, of the integrated optical bench with collimator and camera assemblies, in a thermal altitude environmental chamber on May 29–30, 2014, simulating flight temperature and pressure conditions. BIRC obtained flat-field images viewing a target plate placed in front of the entrance window to the collimator, with the target plate at controlled temperature through use of LN2 cooling. The pho-

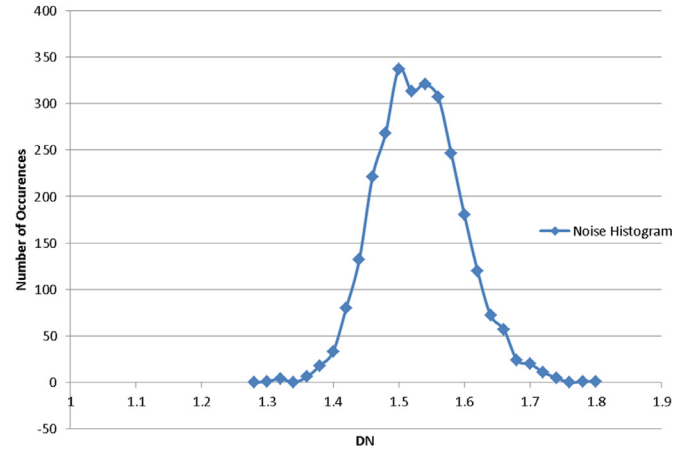


Fig. 8. Read noise histogram. The read noise is 1.52 ± 0.065 DN.

ton transfer method (see Appendix A.4) was used to determine the read noise and the photon transfer characteristic (numbers of photoelectrons detected versus readout digital number DN), by viewing spatially uniform illumination and analyzing image noise statistics versus detected signal levels.

The read noise of the BIRC H2RG/SIDECAR was obtained from analysis of 6580 image acquisitions under temperature and pressure conditions closest to flight conditions (Appendix A.4). The read noise histogram from these images is shown in Fig. 8. The read noise is 1.52 ± 0.065 DN, which is generally much less than the shot noise and other noise sources in the BOPPS data.

The gain of the BIRC H2RG/SIDECAR, meaning the ratio of detected photoelectrons to DN, is a non-linear function of DN. The gain characteristic from the photon transfer test is plotted in Fig. 9, and the gain $G(\text{DN})$ as a function of DN is fitted to the analytic function

$$G(\text{DN}) = E1 * \exp\left(-\frac{\text{DN}}{E2}\right) \quad (4)$$

$$E1 = 38.957853; E2 = 2344.65846 \quad (5)$$

The fitted non-linear gain G , in electrons per DN, is 39.0 e-/DN at 5 DN. It increases to reach $G = 40.7$ e-/DN at 100 DN. The gain increases more rapidly through the upper part of the dynamic range, reaching $G = 73.9$ e-/DN at 1500 DN.

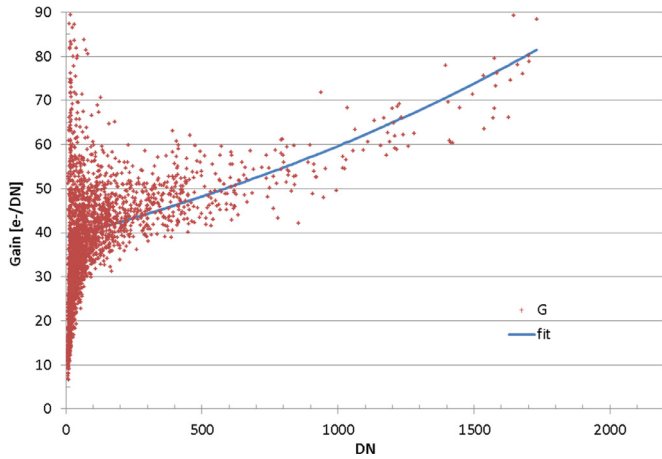


Fig. 9. Determination of detector gain by photon transfer method, from image set 70. Red points are measured gain values; blue curve is least-squares fitted gain characteristic.

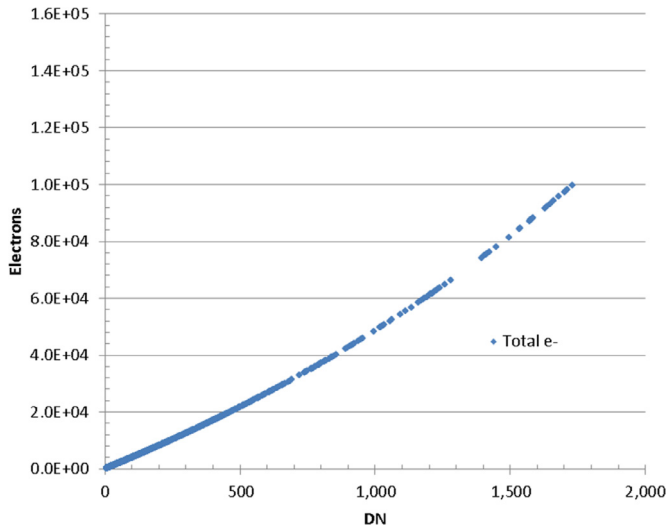


Fig. 10. The BIRC photon transfer characteristic, the cumulative number of photoelectrons detected versus DN.

The conversion of DN in a pixel to the number of photoelectrons counted is obtained by integration of $G(\text{DN})$ from zero to DN. The analytic function $G(\text{DN})$ is integrated to generate the number S of detected photoelectrons versus DN, that is

$$S = 91,342.858 * \exp\left(-\frac{\text{DN}}{2344.65846}\right) - 91,342.858 \quad (6)$$

This photon transfer characteristic is plotted in Fig. 10. A total of $1e5$ photoelectrons have been detected at 1734 DN, giving an average gain of 57.7 e^-/DN . There does not appear to be a well-defined cut-off at full well, but the non-linearity is exponentially increasing, and the full well is placed nominally at $1e5$ electrons. The maximum SNR, considering read noise and shot noise, is ~ 350 near full well (Fig. 11).

A.4. Photon transfer test

The BIRC photon transfer test was performed on May 29–30, 2014 in a thermal-altitude environmental chamber. Test images were acquired in sets, each of which had 654 images, using a scripted test sequence. The photon transfer analysis used sets 34 and later, since the earlier sets had an incorrect skew setting which

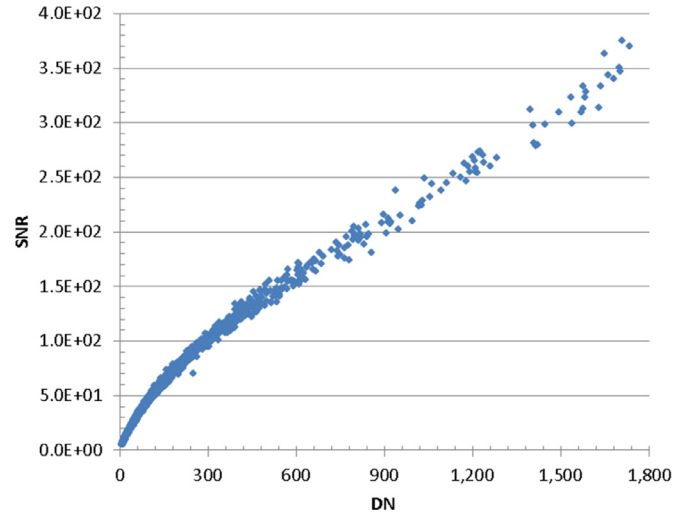


Fig. 11. Signal-to-noise ratio SNR from photon transfer test, including read noise and shot noise.

produced noticeably increased noise in the images. The test images are flat field exposures viewing a target plate at various temperatures. Test conditions were as follows, in the altitude chamber which maintained pressure conditions at 120 kft. The target was an LN_2 -cooled Al plate painted black with Z306, located in front of the collimator entrance window. A non-painted Al baffle extended from the plate to this window, thermally tied to the plate. Instrument temperatures were: optics ~ 190 K, filter wheel housing ~ 114.6 K, ASIC ~ 128.1 K, detector sensor chip assembly ~ 73.9 K, and inner sanctum ~ 69.01 K. The window temperature was varied from $+15$ C to -20 C.

The objectives of the photon transfer test are to determine:

- read noise
- photon transfer characteristic (numbers of photoelectrons detected versus DN)

The photon transfer test also yields an experimental determination of SNR. Results of the photon transfer analysis are summarized here while additional background information on the photon transfer method is given in the next section.

The BIRC instrument operation is such that each commanded image acquisition produces two image frames, where one frame has the commanded exposure and the other is a bias frame (which actually also includes a 3.48 ms exposure). In usual operation the bias frame is subtracted from the exposure frame. For the photon transfer test, a pair of commanded image acquisitions is taken at each desired exposure time, producing a total of four frames, comprising two bias frames and two exposed frames. The two bias frames are used to determine the read noise. The two exposed frames are used to determine gain.

The photon transfer method was used to determine the detector gain defined as the number of photoelectrons detected per DN, versus DN. This method used flat-field images (with spatially uniform illumination) and analyzed the noise statistics versus the detected signal level. Varying detected signal levels are needed for a photon transfer test and are achieved primarily by using a range of exposure times in each image set. The level of illumination, determined by target plate temperature and instrument window temperatures, needs to be held stable during the time required to acquire the two images (four frames) for each G value. The target plate and instrument window temperatures were varied over a range of predicted environmental conditions. Specifically, for the photon transfer test the filter wheel housing, detector sensor chip

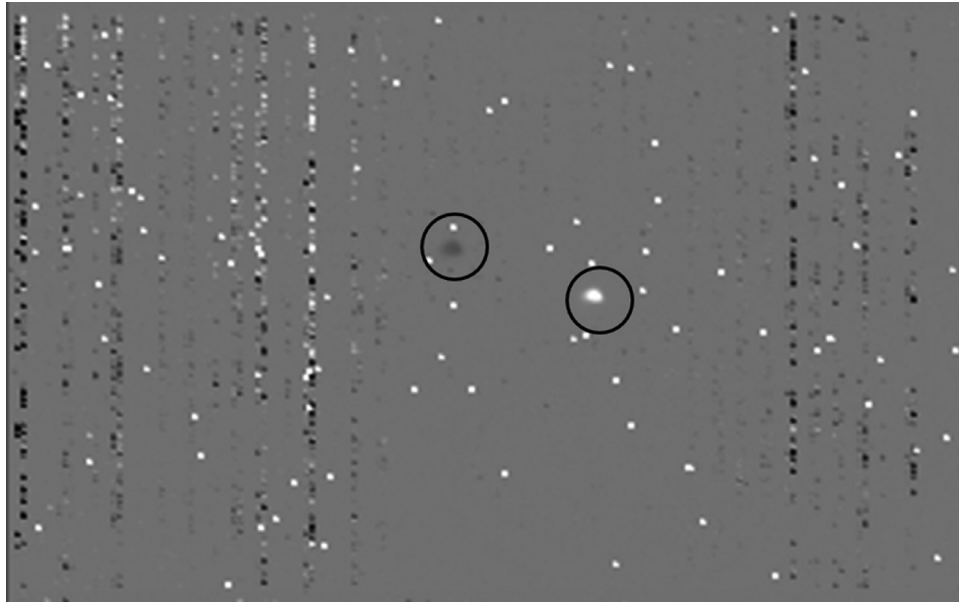


Fig. 12. Shifted, co-added and flatfielded image, highly stretched, showing within black circles the image of Ceres in R band (bright spot) and the negative image (dark spot) produced by the flatfield. The noise aligned in columns arises from skew, which was adjusted in flight shortly after these data were taken.

assembly, ASIC and inner sanctum temperatures were kept stable, but the target plate and instrument window temperatures were slowly varying. The photon transfer test gave no indication of separate photon transfer characteristics in different filters.

Noise statistics are analyzed within a single window for each frame in the photon transfer analyses, so that each pair of image acquisitions (that yielded two bias frames and two commanded exposure frames) produces a single point in a plot of gain vs. DN (e.g., Fig. 9). The window used for these analyses is a 20×20 pixel square with the upper left pixel located at $x = 165$, $y = 128$ (square size and corner locations in pixel units; with [0,0] at upper left). The window is within the illuminated FOV and is chosen to avoid pupil ghosts seen in long wavelength filters. Noise and bad pixels were rejected by deleting pixel values more than 3 sigma from the mean.

Results from image sets 70–79 are plotted in Figs. 8 and 9. This image set was selected for the photon transfer analysis because the temperature and pressure conditions during this portion of the altitude chamber test were the closest to those during flight. The frequency histogram of read noise is shown in Fig. 8, which gives the number of occurrences of a given read noise value determined from a pair of bias frames. The read noise is 1.52 ± 0.065 DN.

Fig. 9 shows the gain measurements, where each measured G value (red points) was obtained from a pair of commanded exposures from the image sets 70–79 which comprised 6580 image acquisitions (saturated images were removed). The resulting non-linear gain characteristic $G(DN)$ is written in Eqs. (4) and (5). The conversion from DN in a pixel, to the number of photoelectrons counted, is obtained by integration of the function $G(DN)$ from zero to the measured DN, see Eq. (6).

A.5. Photon transfer method

The fundamental model of image noise adopted here (Janesick 2007) considers three noise sources, read noise, shot noise, and fixed pattern noise, that are independent and added in quadrature. Read noise is independent of signal level, shot noise is proportional to the square root of signal, and fixed pattern noise is proportional to signal. These different dependences on signal level

are used in a photon transfer test to separate the noise sources, by analyzing how the signal variances change with signal level.

Photon shot noise arises because for a steady illumination source, the arrival times of photons on the detector obey Poisson statistics. The mean count rate of photons arriving on the detector per sec is the same as the variance of the count rate. Hence the rms noise varies as the square root of the signal. On a log-log plot of shot noise versus signal, the shot noise plots as a line of slope $\frac{1}{2}$. At low signal levels, the shot noise becomes small and is usually dominated by read noise which is independent of signal. If the fixed pattern noise is low enough, there is a distinct region at intermediate signal level where shot noise dominates, and here the slope is $\frac{1}{2}$. At higher signal levels, the fixed pattern noise often dominates the shot noise and produces another linear region with slope = 1 (assuming the detector has not yet saturated).

However, such clearly defined regimes do not always appear for detectors, depending on the read noise, fixed pattern noise, and saturation characteristics. In the more general case, the fundamental noise model gives the total rms noise as:

$$\sigma_{TOTAL} = (\sigma_{READ}^2 + \sigma_{SHOT}^2 + \sigma_{FIXPATTERN}^2)^{1/2}$$

The photon transfer method applies this noise model in order to:

- Measure read noise
- Measure ADC gain, written G , in electrons/DN
- Estimate full well

The fixed pattern noise is not an objective of this test and is therefore removed to the extent possible. This is accomplished by taking images in pairs under identical conditions (with identical signals, but two realizations of the noise sampled from the same distribution). Here the images of a pair are subtracted from each other to remove fixed pattern noise.

The pairs of images for the photon transfer test are taken with a constant, flat-field source at a variety of exposure levels, ranging from close to saturation level to less than 10% of saturation. At least several exposure levels, logarithmically spaced within that interval (the linear response region of the detector), are needed. In addition, it is necessary to identify the ‘bad’ pixels, meaning those

whose responsivities are abnormally high or abnormally low, and to remove these pixels from the photon transfer analysis.

The total read noise σ_{READ} in units of DN is measured using pairs of ‘bias frames’, which are taken with zero signal. For BIRC, there are no true bias frames because the H2RG is not operated in any mode where there is zero exposure to foreground signal. The detector has masked rows and columns, and these (or portions of these) are returned with every frame, but the H2RG does not have detectors in its masked rows and columns, so they are not usable for bias frames.

Instead, frames with the minimum possible exposure of 3.48 ms are used as bias frames. The H2RG is operated such that one of these minimum exposure image frames is acquired just before every commanded exposure frame, and both frames are stored. The commanded exposure frame is subtracted from the minimum exposure frame for bias correction and to invert the DN values such that larger DN indicates higher signal strength. The noise from these minimum exposure frames is effectively the read noise given how BIRC is operated, although it includes a small amount of dark current and thermal self-emission as well as foreground signal.

A square ‘window’ is defined for the photon transfer analysis of pairs of minimum exposure bias frames taken under identical conditions. The window avoids bad pixels and includes 400 px. Specifically, the window was the 20×20 square with the upper left pixel located at $x = 165$, $y = 128$ (in pixel units; with [0,0] at upper left). Pairs of bias frames were collected under identical conditions to form difference frames by subtracting one member from the other of each bias frame pair. Within the window, the standard deviation σ is found and divided by $\sqrt{2}$ to account for the noise increase from differencing images. A histogram of $\sigma/\sqrt{2}$ values is then produced.

The gain G in electrons/DN refers to the proportionality constant between DN and detected photoelectrons. The fundamental noise model gives the total noise variance (in electrons) as

$$\delta n^2 = \sigma_e^2 + n$$

Here σ_e is the read noise in electrons, related to σ_{READ} by the gain, $\sigma_e = G\sigma_{READ}$, and the second term is the mean number of electrons which is also the variance from shot noise. Fixed pattern noise is neglected. Both sides of this equation are divided by G^2 to obtain

$$\delta S^2 = \sigma_{READ}^2 + \frac{S}{G}$$

Here S is the mean observed signal in DN, related to n by $S = Gn$, and δS^2 is the signal variance expressed in DN^2 . The read noise squared was determined in the previous step from the differenced bias frames. The gain is then

$$G = \frac{S}{\delta S^2 - \sigma_{READ}^2}$$

which is found from pairs of bias-subtracted image frames taken under identical flat-field illumination. From each image pair, an average frame is created as well as a difference frame. The average DN value S , and the standard deviation of DN in the difference frame (divided by $\sqrt{2}$), are then respectively determined to obtain the gain G .

The signal-to-noise ratio SNR including only read noise and shot noise is found from $S/\delta S$ by

$$SNR = \frac{S}{\sqrt{\sigma_{read}^2 + S/G}}$$

References

- A'Hearn, M.F., et al., 2013. Cometary Volatiles and the Origin of Comets. *Ap J* 758, 29. doi:10.1088/0004-637X/758/1/29.
- A'Hearn, M.F., Belton, M.J.S., Delamere, W.A., et al., 2011. EPOXI at Comet Hartley 2. *Science* 332, 1396. doi:10.1126/science.1204054.
- Adams, J.D., et al., 2015. Balloon Observation Platform for Planetary Science IAC-15-A3.4.10.
- A'Hearn, M.F., Schleicher, D.G., Feldman, P.D., Millis, R.L., Thompson, D.T., 1984. Comet Bowell 1980b. *Astron. J* 89, 579–591.
- Bockelee-Morvan, D., Crovisier, J., Mumma, M.J., Weaver, H.A., 2004. The composition of cometary volatiles. In: Festou, M., Keller, H., Weaver, H. (Eds.), *Comets II*. Univ of Az Press, Tucson, pp. 391–423.
- Bockelee-Morvan, D., Crovisier, J., 1989. The nature of the 2.8- μ m emission feature in cometary spectra. *A&A* 216, 278.
- Bodewits, D., Kelley, M., Li, J.-Y., Farnham, T., A'Hearn, M.F., 2015. The pre-perihelion activity of dynamically new comet C/2013 A1 (Siding Spring) and its close encounter with Mars. *Ap. J. Lett.* 802, L6.
- Brasser, R., Morbidelli, A., 2013. Oort cloud and scattered disc formation during a late dynamical instability in the solar system. *Icarus* 225, 40–49.
- Cheng A.F., Hibbitts C.A., Bernasconi P., and Young E.F. 2015. BOPPS rapid response planetary science: first results. 46th LPSC, 1409.pdf.
- Cheng, A.F., 2015. A Stratospheric Balloon Platform for Rapid Response Comet Images. *SPIE* doi:10.1117/2.1201411.005695.
- Crismani, M.J., et al., 2015. Ultraviolet observations of the hydrogen coma of comet C/2013 A1 (Siding Spring) by MAVEN/IUVS. *Geophys. Res. Lett.* 42, 8803–8809. doi:10.1002/2015GL065290.
- De Sanctis, M.C., et al., 2015. Ammoniated phyllosilicates with a likely outer solar system origin on (1) Ceres. *Nature* 528, 241–244. doi:10.1038/nature16172.
- Gehrz, R.D., Ney, E.P., 1992. 0.7- to 23- μ m photometric observations of P/Halley 1986 III and six recent bright comets. *Icarus* 100, 162–186.
- Gomes, R., Levison, H.F., Tsiganis, K., Morbidelli, A., 2005. Origin of the cataclysmic late heavy bombardment period of the terrestrial planets. *Nature* 435, 466.
- Hanner, M.S., et al., 1997. Thermal emission from the dust coma of Comet Hale-Bopp and the composition of the silicate grains. *Earth, Moon Planets* 79, 247–264.
- Hibbitts C.A. et al. 2015. Characterizing the hydration absorption feature on Ceres using the BOPPS infrared camera. 46th LPSC, 2928.pdf.
- Janesick, J.R., 2007. *Photon Transfer, Volume PM170*. SPIE ISBN 9780819467225.
- Jorda, L., Crovisier, J. and Green D.W.E. 2008. The correlation between visual magnitudes and water production rates. *Asteroids, Comets, Meteors* paper number 8046.
- Kelley, M.S., Wooden, D.H., 2009. The composition of dust in Jupiter-family comets inferred from infrared spectroscopy. *Planetary Space Sci.* 57, 1133–1145.
- Kremic, T., Hibbitts, K., Young, E., Landis, R., Noll, K., Baines, K., 2013. Assessing the potential of stratospheric balloons for planetary science. *IEEEAC Paper #2074*, 2013 IEEE Aerospace Conference March 2–9.
- Kremic, T., et al., 2015. Stratospheric balloons for planetary science and the balloon observation platform for planetary science (BOPPS) mission summary. *IEEE* 978-1-4799-5380-6/15.
- Kueppers, M., et al., 2014. Localized sources of water vapour on the dwarf planet (1) Ceres. *Nature* 505, 525. doi:10.1038/nature12918.
- Levison, H.F., Duncan, M.J., Brasser, R., Kaufmann, D.E., 2010. Capture of the Sun's Oort cloud from stars in its birth cluster. *Science* 329, 187–191.
- Lisse, C.M., et al., 1998. Infrared observations of comets by COBE. *Ap. J.* 496, 971–991.
- Lisse, C.M., et al., 2007. Comparison of the composition of the Tempel 1 ejecta to the dust in comet C/Hale Bopp 1995 O1 and YSO HD 100546. *Icarus* 191, 223–240.
- McMichael, R.T., et al., 2014. Ground-based and Airborne Telescopes V. In: Larry, M.Stepp, Gilmozzi, Roberto, Hall, Helen J (Eds.), *Proc. of SPIE*, Vol. 9145 doi:10.1117/12.2057619, 91452W.
- Morbidelli A., Levison H.F., Tsiganis K., Gomes R. 2005. Chaotic capture of jupiter's trojan asteroids in the early solar system *Nature* 435:462.
- Mumma, M.J., Charnley, S.B., 2011. The Chemical composition of comets—emerging taxonomies and natal heritage. *Ann. Rev. Astron. Astrophys* 49, 471–524 2011.
- Ootsubo, T, et al., 2012. AKARI near-infrared spectroscopic survey for CO₂ in 18 comets. *Ap J* 752, 15. doi:10.1088/0004-637X/752/1/15, 2012.
- Rivkin, A.S., Volquardsen, E., Clark, B., 2006. The surface composition of ceres: discovery of carbonates and iron-rich clays. *Icarus* 185, 563. doi:10.1016/j.icarus.2006.08.022.
- Tsiganis, K., Gomes, R., Morbidelli, A., Levison, H.F., 2005. Origin of the orbital architecture of the giant planets of the solar system. *Nature* 435, 459.
- Vernazza, P., et al., 2005. Analysis of near-IR spectra of 1 Ceres and 4 Vesta, targets of the Dawn mission. *Astron. Abst. Serv.* 436, 1113. doi:10.1051/0004-6361:20042506.
- Wenger, M., et al., 2000. The SIMBAD astronomical database. the CDS reference database for astronomical objects. *Astron. Abstr. Serv.* 143, 9–22.
- Yang, B., Jewitt, D., Bus, S.J., 2009. Comet 17P/Holmes in outburst: the near infrared spectrum. *Astron. J.* 137, 4538–4546. doi:10.1088/0004-6256/137/5/4538.